

Suppression of the skyrmion Hall effect in synthetic ferrimagnets with gradient magnetization

Lan Bo ^{1,2}, Xichao Zhang ², Masahito Mochizuki ^{2,*} and Xuefeng Zhang^{1,3,†}

¹Key Laboratory for Anisotropy and Texture of Materials (MOE), School of Materials Science and Engineering, Northeastern University, Shenyang 110819, China

²Department of Applied Physics, Waseda University, Okubo, Shinjuku-ku, Tokyo 169-8555, Japan

³Institute of Advanced Magnetic Materials, College of Materials and Environmental Engineering, Hangzhou Dianzi University, Hangzhou 310012, China



(Received 18 March 2024; accepted 26 April 2024; published 22 May 2024)

Magnetic skyrmions are promising building blocks for future spintronic devices. However, the skyrmion Hall effect (SkHE) remains an obstacle for practical applications based on the in-line transport of skyrmions. Here, we numerically study the static properties and current-driven dynamics of synthetic ferrimagnetic skyrmions. Inspired by graded-index magnonics, we introduce a linear gradient of saturation magnetization (M_s) in the skyrmion-hosting sample, which effectively modulates the skyrmion Hall angle and suppresses the SkHE. Micromagnetic simulations reveal that ferrimagnetic skyrmions could exhibit greater susceptibility to the variation of M_s as compared to their ferromagnetic counterparts. The Thiele analysis is also applied to support the simulation results, which elucidates that the M_s gradient dynamically modifies the intrinsic normalized size of skyrmions, consequently impacting the SkHE. Our results pave the way to the graded-index skyrmionics, which offers novel insights for designing ferrimagnet-based skyrmionic devices.

DOI: [10.1103/PhysRevResearch.6.023199](https://doi.org/10.1103/PhysRevResearch.6.023199)

I. INTRODUCTION

Magnetic skyrmions are topologically nontrivial spin textures [1–5] characterized by an integer topological charge number $Q = (4\pi)^{-1} \iint \mathbf{m} \cdot (\partial_x \mathbf{m} \times \partial_y \mathbf{m}) d^2r$ [2], and hold great potential as nonvolatile information carriers in next-generation classical and quantum spintronic devices [6–18]. Although the skyrmionics field has predominantly focused on skyrmions in ferromagnetic (FM) materials since their initial experimental observation [19], challenges may arise from the skyrmion Hall effect (SkHE) when driving FM skyrmions by spin currents [20–26]. This effect leads to a transverse motion due to the Q -dependent Magnus force [2], often resulting in undesired accumulation and annihilation of skyrmions at device edges [27,28]. A promising avenue to avoid the SkHE involves the use of antiferromagnetic (AFM) skyrmions [29–47]. While AFM skyrmions exhibit diminished SkHE [32] and potential for fast spin dynamics [48], their insensitivity to external stimuli, such as the magnetic field, limits the manipulation and detection [49].

A balanced solution is to construct the ferrimagnetic (FiM) skyrmions [49–58], which could combine advantages from both FM and AFM materials [49]. It has been demonstrated

that FiM skyrmions exhibit a reduced small but nonzero SkHE [52,58]. An example of FiM skyrmions can be found in the synthetic FiM system based on rare-earth-transition-metal (such as Gd-Co) alloys [52–54,57] or multilayers [58–61], which has garnered significant interest in recent years. In such a system, the two FM components are antiferromagnetically coupled with a bilinear surface exchange interaction [62].

Following the principles inspired by graded-index optics [63], researchers have proposed a continuous modulation of magnetic parameters in spintronics [64–66]. Although previous studies have delved into scenarios involving magnetic anisotropy gradients [67–69] and Dzyaloshinskii-Moriya interaction (DMI) gradients [70–72] to control skyrmion dynamics, models with saturation magnetization (M_s) gradients have only been extensively investigated in the context of magnonics [73–77], but have not yet been explored in the study of skyrmion dynamics. The M_s of FiM materials exhibits higher sensitivity to temperature changes compared to that of FM materials, which provides a natural advantage in constructing M_s gradients through thermal landscapes [78,79].

In light of the current fervor in both FiM skyrmions and graded-index spintronics, in this work, we numerically investigate the skyrmion dynamics in synthetic FiM with a M_s gradient. It is demonstrated that introduction of the M_s gradient can effectively regulate the skyrmion Hall angle. A theoretical analysis further reveals that the regulation is attributed to the variation of normalized skyrmion radius. The paper is organized as follows. In Sec. II, we describe the micromagnetic and analytical model. In Sec. III, we show and discuss the results of the numerical studies, which are summarized in Sec. IV. Specifically, in Sec. III A, we

*Corresponding author: masa_mochizuki@waseda.jp

†Corresponding author: zhang@hdu.edu.cn

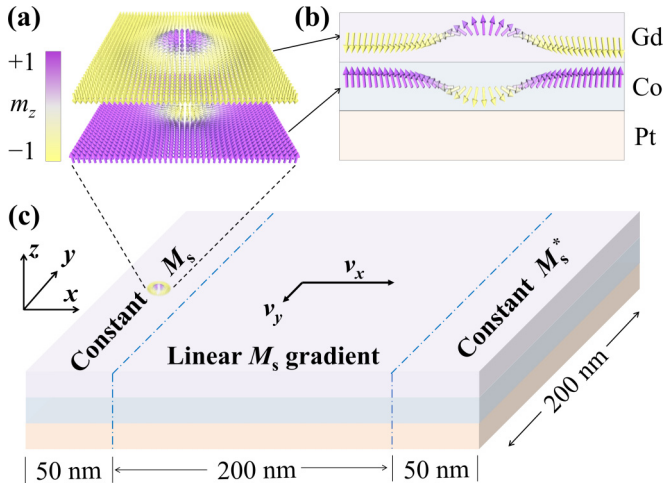


FIG. 1. (a) Schematic configuration of a ferrimagnetically exchange-coupled bilayer skyrmion. Arrows represent the magnetization, and the color represents their z component m_z . (b) Cross-sectional view of the Gd/Co/Pt heterojunction. Only the magnetization in free layers is explicitly modeled. (c) Schematic diagram of the geometry for skyrmion dynamics. The central region has a linear magnetization gradient ΔM_s , and the left and right regions have constant M_s .

verify how static skyrmion configuration varies with changes in material parameters, preparing for subsequent dynamic studies. In Sec. III B, two types of current injection geometries are compared, and an overall trajectory of skyrmion motion induced by spin-orbit torque (SOT) is provided. The details of skyrmion dynamics are presented, demonstrating an effective suppression of SkHE in the presence of the M_s gradient. In Sec. III C, we analyze the physical mechanisms behind the simulation results based on the Thiele approach.

II. MODEL AND METHODOLOGY

The system considered in our simulations is a synthetic FiM Gd/Co/Pt multilayer [58–61]. As depicted in Figs. 1(a) and 1(b), the magnetizations in Gd and Co layers are oppositely aligned due to the AFM coupling, leading to the opposite polarities of skyrmions in the two layers. This kind of magnetization configuration is known as the exchange-coupled bilayer skyrmion [37,41,58]. As shown in Fig. 1(c), a nanoplate geometry with dimensions of 300×200 nm is considered to investigate skyrmion dynamics. This nanoplate includes regions at the left and right sides with constant M_s values (i.e., M_s and M_s^*), each spanning a width of 50 nm. In the central square region of 200×200 nm, spatially varying M_s values with a linear gradient ΔM_s are introduced along the x axis. Periodic boundary conditions are imposed in the y direction to remove the potential boundary effect. With a single isolated skyrmion initially placed at the left side, a spin-polarized current is applied to drive this skyrmion into motion toward the $+x$ direction.

The total Hamiltonian H of the system includes intralayer terms H_{intra}^L for respective layers ($L = \text{Co}, \text{Gd}$) and an

interlayer term H_{inter} , which is given by

$$H = H_{\text{intra}}^{\text{Co}} + H_{\text{intra}}^{\text{Gd}} + H_{\text{inter}}. \quad (1)$$

The intralayer Hamiltonian for each layer reads

$$H_{\text{intra}}^L = -A \sum_{\langle i,j \rangle} \mathbf{m}_i^L \cdot \mathbf{m}_j^L + K \sum_i [1 - (\mathbf{m}_i^{L,z})^2] + D_{ij} \sum_{\langle i,j \rangle} (v_{ij} \times \hat{z}) \cdot (\mathbf{m}_i^L \times \mathbf{m}_j^L) + H_d, \quad (2)$$

where $|\mathbf{m}_i^L| = 1$ represents the normalized local magnetic moment at site i , and $\langle i, j \rangle$ extends to all the nearest-neighbor sites in each layer. The first term represents the FM Heisenberg exchange interaction with A being the intralayer exchange constant. The second term represents the perpendicular magnetic anisotropy (PMA) with K being the anisotropy constant. The third term represents the DMI, where D_{ij} is the DMI constant and v_{ij} is the unit vector between sites i and j . The fourth term H_d represents the dipole-dipole interaction. On the other hand, the interlayer Hamiltonian which describes the interaction between Co and Gd layers reads [31]

$$H_{\text{inter}} = -\sigma c_z \sum_i \mathbf{m}_i^{\text{Co}} \cdot \mathbf{m}_i^{\text{Gd}}, \quad (3)$$

where c_z is the thickness of the cell size, and σ is the bilinear surface exchange coefficient.

To explore the current-induced dynamics of the FiM skyrmion, we numerically solve the Landau-Lifshitz-Gilbert (LLG) equation augmented with a spin-torque term τ ,

$$\partial_t \mathbf{m} = -\gamma \mathbf{m} \times \mathbf{h}_{\text{eff}} + \alpha (\mathbf{m} \times \partial_t \mathbf{m}) + \tau, \quad (4)$$

where γ is the gyromagnetic ratio, α is the Gilbert damping coefficient, and $\mathbf{h}_{\text{eff}} = -(\partial H / \partial \mathbf{m}) / (\mu_0 M_s)$ is the effective local field with μ_0 being the vacuum permeability constant. We consider two strategies for the injection of spin-polarized currents [80]. For the current-in-plane (CIP) geometry, the current flows through all the layers where the spin-transfer torques (STTs) are formulated in the Zhang-Li form [81]:

$$\tau_{\text{STT}} = u(\mathbf{m} \times \partial_x \mathbf{m} \times \mathbf{m}) - \beta u(\mathbf{m} \times \partial_x \mathbf{m}). \quad (5)$$

Here, the first term is the adiabatic torque, and the second term is the nonadiabatic torque with β being the degree of nonadiabaticity. The STT coefficient is given by $u = (g\mu_B P J) / (2eM_s)$ [82], where g , μ_B , P , e , and J are the Landé factor, Bohr magneton, spin polarization factor, elementary charge, and applied current density, respectively. On the contrary, for the current-perpendicular-to-plane (CPP) geometry, the charge current flows through the Pt layer and leads to an out-of-plane spin current due to the spin Hall effect [80]. In this case, dampinglike spin-orbit torque (SOT) works, which is formulated as [83]

$$\tau_{\text{SOT}} = \left(\frac{g\mu_B \theta_H J}{2ec_z M_s} \right) (\mathbf{m} \times \mathbf{m}_p \times \mathbf{m}), \quad (6)$$

where θ_H is the spin Hall angle and \mathbf{m}_p is the normalized spin polarization vector. Here, the fieldlike SOT is excluded as its impact on the skyrmion dynamics is negligible [37].

The simulations are performed by MuMax3 finite-difference GPU accelerated code [84]. The simulation volumes for static and dynamic cases are $100 \times 100 \times 1$ nm³ and

TABLE I. Simulation parameters.

Parameters	Units	Co layer	Gd layer	References
M_s^a	MA/m	1.44	0.72	[60,85]
A	pJ/m	15 [5,20] ^b		[62]
K	MJ/m ³	2.0 [1.5, 3.0]	0	[86]
D	mJ/m ²	2.5 [1.5, 3.0]	0	[62]
σ	mJ/m ²	-10		[32]
α		0.02		[23,57]
g^c		2.2	2.0	[57]
J	GA/m ²	1 [0.1, 10]		[32]
P		0.4		[37]
θ_H		0.05		[87]
ΔM_s		[-0.05, 0.05]		

^aFor simplify, M_s^{Gd} is always set to an estimated value of 50% of M_s^{Co} [60].

^bValues enclosed in square brackets denote the ranges of variation.

^cFor simplify, an average value of $g = 2.1$ is employed for both layers.

$300 \times 200 \times 1 \text{ nm}^3$, respectively, with a cell size of 0.5 nm , matching the lattice constant of Co to maximize the calculation accuracy. The default simulation parameters and their ranges of variation are given in Table I.

III. RESULTS AND DISCUSSION

A. Static FiM skyrmion without a M_s gradient

We begin by verifying the configuration of a static FiM skyrmion in a system without a M_s gradient. For this purpose, we utilize a square geometry system of $100 \times 100 \text{ nm}^2$ with infinite boundaries. A bilayer skyrmion is initialized in the system and the equilibrium state is then determined using the conjugate gradient method. First, while maintaining the default M_s , we investigate the impact of variation in material parameters A , D , and K on the stability and size of the skyrmion. The results are depicted in Figs. 2(a)–2(c), where in each figure two parameters are varied with the remaining parameter being fixed at its default value. Overall, the skyrmion radius R varies from a few nanometers to approximately 30 nm within the selected range, which is positively correlated with D , while negatively correlated with A and K . When skyrmion size becomes excessively large or small, the system tends to change into multidomain or uniform states. It is noteworthy that the stability of skyrmions does not necessarily require such a large PMA because similar configurations can be obtained by applying a vertical external magnetic field [88]. Based on the above results, we set $A = 15$, $D = 2.5$, and $K = 2.0$ as default values, resulting in an initial skyrmion radius of 5.5 nm .

Second, we fix A , D , and K at their default values and vary M_s within a small range of $\pm 5\%$ (i.e., M_s^{Co} ranging from 1.386

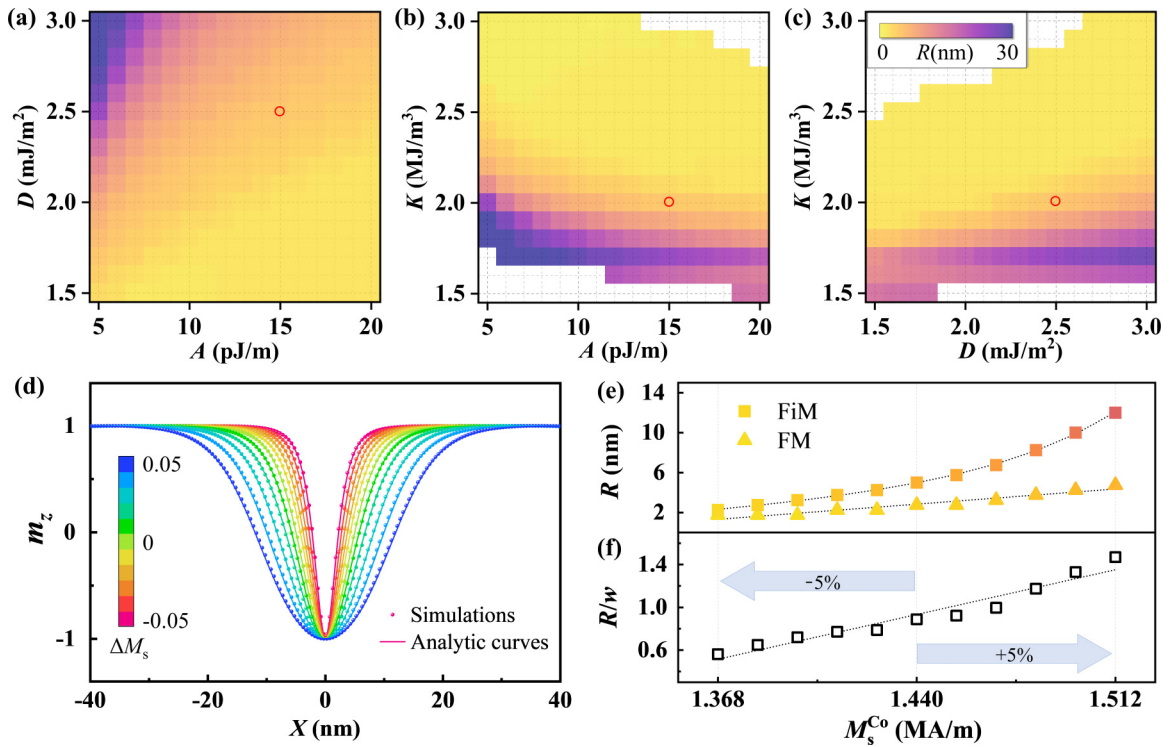


FIG. 2. (a)–(c) Variations of equilibrium skyrmion radius R versus material parameters A , D , and K . The color represents the skyrmion size, and the white region indicates the absence of a stable skyrmion. The red circles mark the situation with default parameters, i.e., $K = 2.0$, $D = 2.5$, and $A = 15$. (d) Magnetization component m_z plotted as a function of position X along the skyrmion diameter under different M_s . The symbols are simulation results, and the solid lines are fitted curves. (e) Variations of skyrmion radius R for both FM and FiM cases versus M_s . (f) Variations of the ratio of skyrmion radius to domain wall width R/w versus M_s . The symbols are simulation or analytical results, and the dashed lines are used to guide the eyes.

to 1.512 while M_s^{Gd} maintains half of the M_s^{Co} value) [60] to observe variation in the skyrmion configuration. The m_z profiles along the diameter direction under different M_s are depicted in Fig. 2(d). The dots are extracted from simulation data, while the solid curves are results of fitting with [86]

$$m_z(X) = 2 \tan^{-1} \left[\frac{\sinh(R/w)}{\sinh(X/w)} \right], \quad (7)$$

where w is the width of the 360° domain wall of the skyrmion, considered as a fitting parameter, and R/w is the normalized skyrmion radius. Given that our simulation results agree well with the theoretical formula, we thus extract R and R/w from Fig. 2(d) and plot their variations with respect to M_s in Figs. 2(e) and 2(f). For comparison, calculated values of R in a single-layer FM are also plotted, where a notably higher sensitivity of FiM skyrmion size to M_s is observed. Note that R/w also increases with increasing M_s , and approximately exhibits a linear relationship, which has an important meaning in the subsequent theoretical analysis (see Sec. III C).

B. Suppression of the skyrmion Hall effect

We first consider the case with constant M_s . As described in Sec. II, both CPP and CIP injection geometries are initially considered for current-driven skyrmion motion. For CIP injection, we further examine two cases with different nonadiabatic degrees, $\beta = 0$ and $\beta = \alpha$. The dependence of skyrmion velocity $v = \|\mathbf{v}\|$ on the current density J for different scenarios is shown in Fig. 3(a). The overlapping symbols indicate that skyrmions in the two layers always move as bounded entities. This means that the interlayer surface exchange σ is sufficiently strong, thereby preventing their decoupling under high current. Moreover, the CPP injection turns out to be of much greater efficiency in driving skyrmions compared to the CIP injection, which is consistent with reported findings on FM skyrmions [80] and AFM skyrmions [32]. Therefore, in the following sections, we only consider the SOT-induced skyrmion motion for the sake of simplicity, with a moderate density of 1 GA/m^2 .

Next, we introduce the M_s gradient in the central region of the nanoplate. The linear ΔM_s is defined as

$$\Delta M_s = (M_s^* - M_s) / M_s, \quad (8)$$

where ΔM_s varies between ± 0.05 and is controlled by changing M_s^* at the right-side region. For various values of ΔM_s , snapshots of the driven skyrmions near the left and right markers (yellow chain lines) of the gradient region are presented in Fig. 3(b). At 8.5 ns, the skyrmion reaches the left marker and begins to move along different trajectories under the influence of different ΔM_s . We find significant variations in the skyrmion size and velocity during the moving process. Positive ΔM_s leads to an expansion of the skyrmion and a decrease in velocity, while negative ΔM_s results in its contraction and an increase in velocity. The trajectories of the skyrmion present a scattered distribution. When $\Delta M_s = 0$, there is a small but nonzero skyrmion Hall angle Φ , consistent with a previous report [58]. As ΔM_s varies, the trajectory exhibits a monotonic and regular change, providing visual evidence that the magnetization gradient can regulate the skyrmion Hall angle Φ .

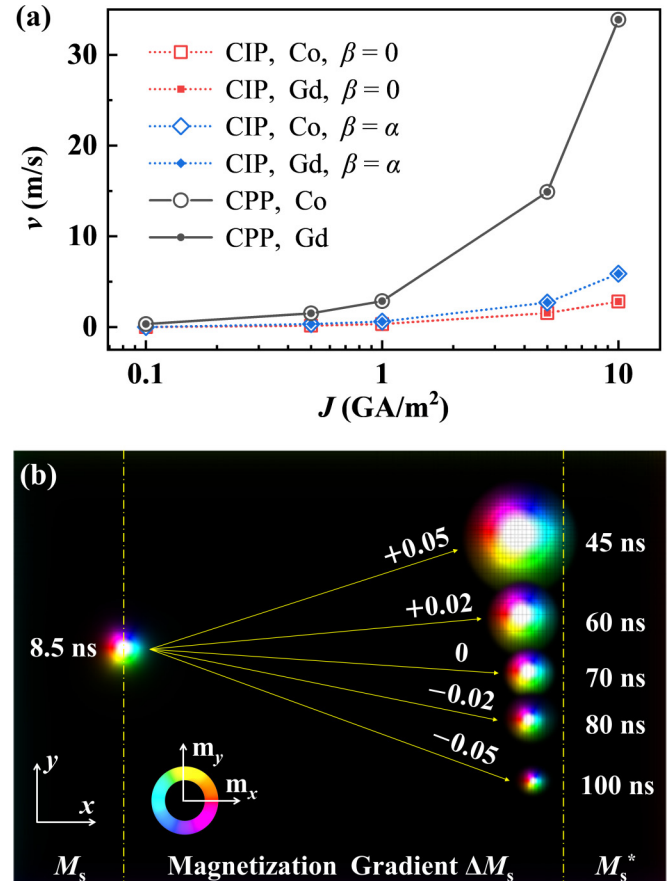


FIG. 3. (a) Skyrmion velocity v as a function of the driving current density J for both CPP and CIP injections. The Co and Gd layers are represented by hollow and solid symbols, respectively. (b) Snapshots of the SOT-induced skyrmion dynamics for various ΔM_s . The dashed lines separate regions with constant M_s or finite M_s gradient, and the arrows indicate the direction of skyrmion motion. The color wheel indicates the in-plane magnetization. ΔM_s and time information are indicated in white text.

To learn more details of the skyrmion motion under the M_s gradient, we further extract the data of skyrmion dynamics, which display the variations in skyrmion position $Y(X)$, radius R , and velocity components v_x and v_y as functions of the position X in Fig. 4. Here, to provide more precise outcomes, we only display the cases where ΔM_s varies from -0.02 to $+0.03$, within the central gradient range. The skyrmion center is determined by averaging the position coordinates of the 360° domain wall with $m_z = 0$. The results in Fig. 4(a) are similar to those in Fig. 3(b), but we can observe that the trajectories of the skyrmion center are remarkably smooth. It is noteworthy that there is almost no displacement in the y direction when $\Delta M_s = +0.01$. Figure 4(b) reveals linear dependence between R and X with a slope determined by ΔM_s , where positive (negative) ΔM_s tends to induce the expansion (shrinkage) of the skyrmion. Importantly, the dynamically changing values of R agree well with those in the equilibrium states in Fig. 2(e). This agreement is expected when the skyrmion velocity is relatively low because the driven skyrmion can be relaxed to approach the minimal-energy configuration at equilibrium at each moment. Therefore, we

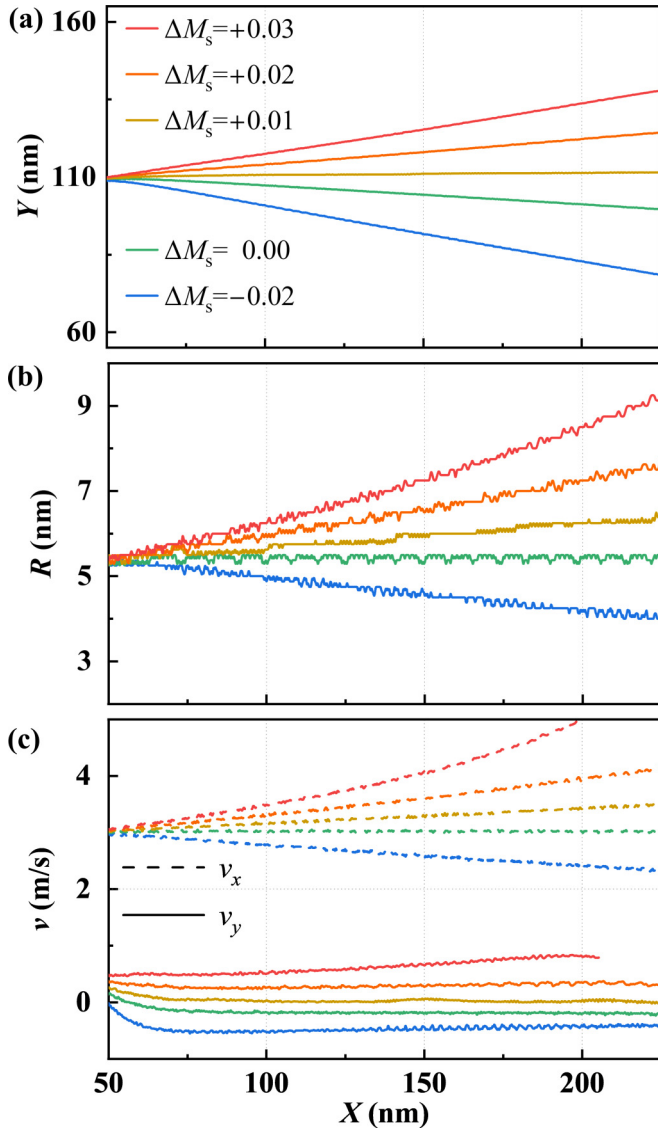


FIG. 4. (a) Variations of the skyrmion center coordinates (X, Y) in the central region during the motion process. (b) Variations of the skyrmion radius R versus position X for various ΔM_s . (c) Variations of the skyrmion velocity components, v_x and v_y , versus position X . The dashed lines represent v_x , and the solid lines represent v_y . The color of the line indicates different ΔM_s .

believe that the findings about the static configuration in Fig. 2(e) are also applicable for the analysis of the driven skyrmions. The velocity components, v_x and v_y , are crucial parameters in determining Φ . Hence, we plot them separately in Fig. 4(c). When ΔM_s is positive (negative), both v_x and v_y increase (decrease) as compared with those at $\Delta M_s = 0$. The difference appears in their spatial-position dependence; that is, v_y is nearly independent of the position, whereas v_x exhibits nearly linear dependence on X .

After obtaining the skyrmion instantaneous velocity $\mathbf{v}(v_x, v_y)$, we can then calculate the skyrmion Hall angle Φ at each moment by

$$\Phi = \tan^{-1}(v_y/v_x). \quad (9)$$

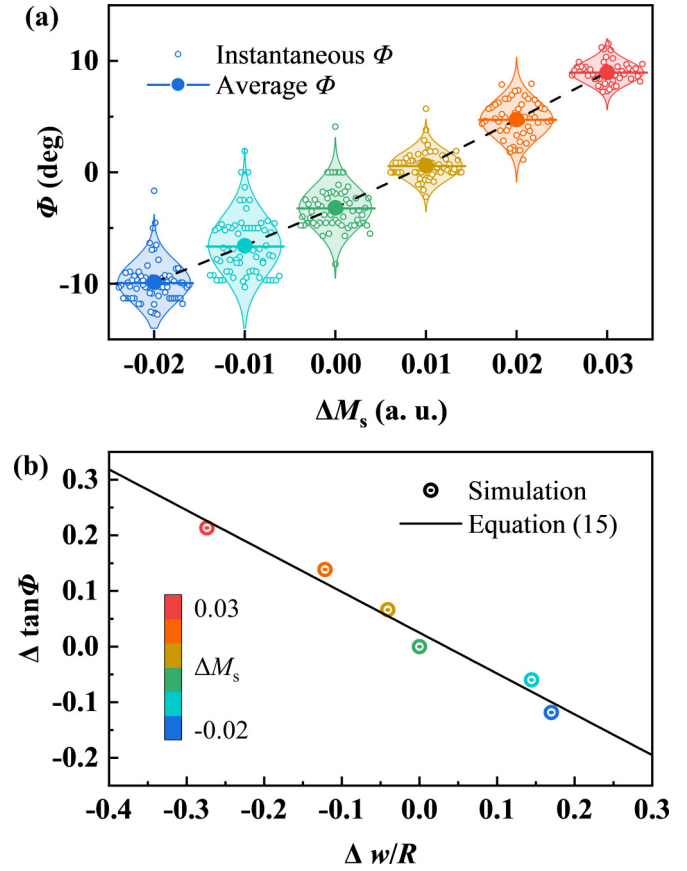


FIG. 5. (a) Violin plot with hollow and solid symbols depicting the instantaneous and average skyrmion Hall angles Φ for various ΔM_s . The side-profile lines represent the probability density distribution of instantaneous values. The dashed line illustrates the variation of Φ versus ΔM_s . (b) The increment of skyrmion Hall angle $\Delta \tan \Phi$ plotted as a function of the increment of the reciprocal of the normalized skyrmion radius $\Delta w/R$. The symbols represent simulation results, with colors indicating various ΔM_s . The solid line is a linear fitted line based on Eq. (15).

As the motion of a skyrmion is a continuous process, we are more interested in its total displacement over a certain period of time. Therefore, we further calculate the average value of Φ throughout the entire motion, presenting it alongside the instantaneous values in Fig. 5(a). Figure 5(a) is a violin plot with the instantaneous and average values of Φ being represented by hollow and solid symbols, respectively. The curves on both sides of the violin shape display the probability density distribution, which clearly indicates a Gaussian distribution for all ΔM_s . When the variation in ΔM_s is within 5% (ranging from -0.02 to $+0.03$), the change in Φ can reach up to $\pm 10^\circ$, and it exhibits an approximately linear correlation with ΔM_s . Specifically, when ΔM_s is $+0.01$, the average value of Φ is only 0.06° , indicating an extremely small SkHE.

C. Analysis based on Thiele equation

In this section, we theoretically analyze of the simulation results. While the size of a Néel skyrmion may change, its central symmetry in shape remains unchanged, which allows us to model it as a rigid pointlike particle. Therefore, its

motion can be qualitatively elucidated by a modified Thiele equation [89],

$$\mathbf{G} \times \mathbf{v} - \alpha \mathcal{D} \cdot \mathbf{v} + \mathcal{B} \cdot \mathbf{J} = \mathbf{0}. \quad (10)$$

The three terms arise from the precessional, damping, and SOT terms in the LLG equation, respectively. Here, $\mathbf{G} = n\hat{z}$ is the gyromagnetic coupling vector, \mathcal{D} is the dissipative tensor, and the tensor \mathcal{B} quantifies the efficiency of the spin Hall torque over the two-dimensional configuration. The parameters n and d correspond respectively to the topological invariant as a sum of the solid angles of magnetizations, and the component of the dissipation tensor as an indicator of the magnetization rotation length scale, given by

$$n = \iint \mathbf{m} \cdot (\partial_x \mathbf{m} \times \partial_y \mathbf{m}) d^2 r, \quad (11)$$

$$d = \mathcal{D}_{xx} = \mathcal{D}_{yy} = \iint (\partial_x \mathbf{m})^2 d^2 r. \quad (12)$$

For a FM skyrmion with a simple profile, d is approximately given by $d \approx \pi^3 R/w$ [23], while for a FiM skyrmion with R roughly as large as w , it is given by $d \approx 2\pi R/w$ [57]. This means that $d \propto R/w$ is expected to scale likewise with the normalized skyrmion radius R/w presented in Fig. 2(e). In our model, due to the presence of spatially dependent ΔM_s , the skyrmion internal configuration R/w changes with X , resulting in the variation of $d = kR/w$ during the skyrmion motion, where k is the proportionality coefficient.

The solutions of Eq. (10) are

$$v_x = B_0 J \left(\frac{\alpha d}{1 + \alpha^2 d^2} \right), \quad (13)$$

$$v_y = B_0 J \left(\frac{n}{1 + \alpha^2 d^2} \right), \quad (14)$$

where B_0 is a constant derived from the tensor \mathcal{B} . Equations (13) and (14) can be used to explain the results of instantaneous velocity in Figs. 4(c) and 4(d). When α is small enough, the term $\alpha^2 d^2$ can be neglected, so that v_y becomes independent of d , manifested in Fig. 4(d) as v_y almost unrelated to X . As for v_x , the term αd cannot be neglected, so that v_x is related to d , i.e., correlated with R/w , as seen in Fig. 4(c), where v_x exhibits an approximate linear correlation with X .

Regarding the variation of the skyrmion Hall angle Φ , it follows the relation

$$\tan \Phi \equiv \frac{v_y}{v_x} = \frac{kn}{\alpha} \cdot \frac{w}{R}. \quad (15)$$

The above Eq. (15) can be used to explain the simulation results shown in Fig. 5(a). The original variable ΔM_s affects the

internal skyrmion configuration R/w , causing an incremental change Δd during the motion process. This further leads to an increment of $\Delta \Phi$. When ΔM_s takes an appropriate value, around +0.01 in this work, $\Delta \Phi$ precisely compensates for the original Φ , thus suppressing the skyrmion Hall effect. To visually demonstrate the relationship in Eq. (15), we plot the function of $\Delta \tan \Phi$ with respect to $\Delta w/R$, as shown in Fig. 5(b). This function reveals the correlation between the changes in Φ and the normalized skyrmion radius. We find that the simulation results for different ΔM_s are uniformly distributed around the theoretical line, and the linear relationship conforms to the description provided by Eq. (15).

IV. CONCLUSION

In conclusion, we have investigated the static properties and current-induced dynamics of the synthetic FiM skyrmions. Compared to the FM skyrmions, equilibrium FiM skyrmions exhibit a higher sensitivity of their static profiles to the variation in M_s . Inspired by the graded M_s in the field of graded-index magnonics, we have explored the influence of a M_s gradient on the skyrmion dynamics by particularly focusing on the SOT-induced motion. It is shown that the presence of a M_s gradient significantly affects the trajectory, velocity, and size of the driven skyrmion. Notably, a 5% variation in the M_s gradient can control the skyrmion Hall angle within a range of $\pm 10^\circ$. Specifically, a 1% M_s gradient completely suppresses the SkHE. We have analyzed the simulation results using Thiele theory, demonstrating that the M_s gradient regulates the skyrmion Hall angle by influencing the normalized skyrmion radius. In this study, we have incorporated the M_s gradient from the magnonics to the skyrmionics. Our findings are expected to provide a new perspective to overcome the SkHE, which has been an obstacle to the technical applications of skyrmions so far.

ACKNOWLEDGMENTS

X.F.Z. acknowledges support by the National Science Fund for Distinguished Young Scholars (Grant No. 52225312), the National Natural Science Foundation of China (Grant No. U1908220), and the Key Research and Development Program of Zhejiang Province (Grant No. 2021C01033). X.C.Z. and M.M. acknowledge support by the JST CREST (Grant No. JPMJCR20T1). M.M. also acknowledges support by the JSPS KAKENHI (Grants No. JP20H00337, No. JP23H04522, and No. JP24H02231), and the Waseda University Grant for Special Research Projects (Grant No. 2024C-153). L.B. acknowledges the financial support by China Scholarship Council (Grant No. 202206080023).

- [1] U. K. Rössler, A. Bogdanov, and C. Pfleiderer, Spontaneous skyrmion ground states in magnetic metals, *Nature (London)* **442**, 797 (2006).
 [2] N. Nagaosa and Y. Tokura, Topological properties and dynamics of magnetic skyrmions, *Nat. Nanotechnol.* **8**, 899 (2013).

- [3] M. Mochizuki and S. Seki, Dynamical magnetoelectric phenomena of multiferroic skyrmions, *J. Phys.: Condens. Matter* **27**, 503001 (2015).
 [4] W. Jiang, G. Chen, K. Liu, J. Zang, S. G. Te Velthuis, and A. Hoffmann, Skyrmions in magnetic multilayers, *Phys. Rep.* **704**, 1 (2017).

- [5] N. Kanazawa, S. Seki, and Y. Tokura, Noncentrosymmetric magnets hosting magnetic skyrmions, *Adv. Mater.* **29**, 1603227 (2017).
- [6] G. Finocchio, F. Büttner, R. Tomasello, M. Carpentieri, and M. Kläui, Magnetic skyrmions: From fundamental to applications, *J. Phys. D* **49**, 423001 (2016).
- [7] W. Kang, Y. Huang, X. Zhang, Y. Zhou, and W. Zhao, Skyrmion-electronics: An overview and outlook, *Proc. IEEE* **104**, 2040 (2016).
- [8] A. Fert, N. Reyren, and V. Cros, Magnetic skyrmions: Advances in physics and potential applications, *Nat. Rev. Mater.* **2**, 17031 (2017).
- [9] K. Everschor-Sitte, J. Masell, R. M. Reeve, and M. Kläui, Perspective: Magnetic skyrmions—overview of recent progress in an active research field, *J. Appl. Phys.* **124**, 240901 (2018).
- [10] Y. Tokura and N. Kanazawa, Magnetic skyrmion materials, *Chem. Rev.* **121**, 2857 (2021).
- [11] C. Back, V. Cros, H. Ebert, K. Everschor-Sitte, A. Fert, M. Garst, T. Ma, S. Mankovsky, T. Monchesky, M. Mostovoy *et al.*, The 2020 skyrmionics roadmap, *J. Phys. D* **53**, 363001 (2020).
- [12] X. Zhang, Y. Zhou, K. M. Song, T.-E. Park, J. Xia, M. Ezawa, X. Liu, W. Zhao, G. Zhao, and S. Woo, Skyrmion-electronics: Writing, deleting, reading and processing magnetic skyrmions toward spintronic applications, *J. Phys.: Condens. Matter* **32**, 143001 (2020).
- [13] A. N. Bogdanov and C. Panagopoulos, Physical foundations and basic properties of magnetic skyrmions, *Nat. Rev. Phys.* **2**, 492 (2020).
- [14] B. Dieny, I. L. Prejbeanu, K. Garello, P. Gambardella, P. Freitas, R. Lehndorff, W. Raberg, U. Ebels, S. O. Demokritov, J. Akerman *et al.*, Opportunities and challenges for spintronics in the microelectronics industry, *Nat. Electron.* **3**, 446 (2020).
- [15] L. Bo, C. Hu, R. Zhao, and X. Zhang, Micromagnetic manipulation and spin excitation of skyrmionic structures, *J. Phys. D* **55**, 333001 (2022).
- [16] C. Psaroudaki and C. Panagopoulos, Skyrmion qubits: A new class of quantum logic elements based on nanoscale magnetization, *Phys. Rev. Lett.* **127**, 067201 (2021).
- [17] C. Psaroudaki, E. Peraticos, and C. Panagopoulos, Skyrmion qubits: Challenges for future quantum computing applications, *Appl. Phys. Lett.* **123**, 260501 (2023).
- [18] J. Xia, X. Zhang, X. Liu, Y. Zhou, and M. Ezawa, Universal quantum computation based on nanoscale skyrmion helicity qubits in frustrated magnets, *Phys. Rev. Lett.* **130**, 106701 (2023).
- [19] X. Yu, Y. Onose, N. Kanazawa, J. H. Park, J. Han, Y. Matsui, N. Nagaosa, and Y. Tokura, Real-space observation of a two-dimensional skyrmion crystal, *Nature (London)* **465**, 901 (2010).
- [20] J. Zang, M. Mostovoy, J. H. Han, and N. Nagaosa, Dynamics of skyrmion crystals in metallic thin films, *Phys. Rev. Lett.* **107**, 136804 (2011).
- [21] J. Iwasaki, M. Mochizuki, and N. Nagaosa, Current-induced skyrmion dynamics in constricted geometries, *Nat. Nanotechnol.* **8**, 742 (2013).
- [22] J. Iwasaki, M. Mochizuki, and N. Nagaosa, Universal current-velocity relation of skyrmion motion in chiral magnets, *Nat. Commun.* **4**, 1463 (2013).
- [23] W. Jiang, X. Zhang, G. Yu, W. Zhang, X. Wang, M. B. Jungfleisch, J. E. Pearson, X. Cheng, O. Heinonen, K. L. Wang *et al.*, Direct observation of the skyrmion Hall effect, *Nat. Phys.* **13**, 162 (2017).
- [24] K. Litzius, I. Lemesch, B. Krüger, P. Bassirian, L. Caretta, K. Richter, F. Büttner, K. Sato, O. A. Tretiakov, J. Förster *et al.*, Skyrmion Hall effect revealed by direct time-resolved x-ray microscopy, *Nat. Phys.* **13**, 170 (2017).
- [25] G. Chen, Skyrmion Hall effect, *Nat. Phys.* **13**, 112 (2017).
- [26] R. Tomasello, A. Giordano, S. Chiappini, R. Zivieri, G. Siracusano, V. Puliafito, I. Medlej, A. La Corte, B. Azzerboni, M. Carpentieri *et al.*, Micromagnetic understanding of the skyrmion Hall angle current dependence in perpendicularly magnetized ferromagnets, *Phys. Rev. B* **98**, 224418 (2018).
- [27] I. Purnama, W. L. Gan, D. W. Wong, and W. S. Lew, Guided current-induced skyrmion motion in 1D potential well, *Sci. Rep.* **5**, 10620 (2015).
- [28] X. Zhang, G. Zhao, H. Fangohr, J. P. Liu, W. Xia, J. Xia, and F. Morvan, Skyrmion-skyrmion and skyrmion-edge repulsions in skyrmion-based racetrack memory, *Sci. Rep.* **5**, 7643 (2015).
- [29] H. D. Rosales, D. C. Cabra, and P. Pujol, Three-sublattice skyrmion crystal in the antiferromagnetic triangular lattice, *Phys. Rev. B* **92**, 214439 (2015).
- [30] J. Barker and O. A. Tretiakov, Static and dynamical properties of antiferromagnetic skyrmions in the presence of applied current and temperature, *Phys. Rev. Lett.* **116**, 147203 (2016).
- [31] X. Zhang, M. Ezawa, and Y. Zhou, Thermally stable magnetic skyrmions in multilayer synthetic antiferromagnetic racetracks, *Phys. Rev. B* **94**, 064406 (2016).
- [32] X. Zhang, Y. Zhou, and M. Ezawa, Magnetic bilayer-skyrmions without skyrmion hall effect, *Nat. Commun.* **7**, 10293 (2016).
- [33] R. Tomasello, V. Puliafito, E. Martinez, A. Manchon, M. Ricci, M. Carpentieri, and G. Finocchio, Performance of synthetic antiferromagnetic racetrack memory: Domain wall versus skyrmion, *J. Phys. D* **50**, 325302 (2017).
- [34] R. Duine, K.-J. Lee, S. S. Parkin, and M. D. Stiles, Synthetic antiferromagnetic spintronics, *Nat. Phys.* **14**, 217 (2018).
- [35] T. Moriyama, W. Zhou, T. Seki, K. Takanashi, and T. Ono, Spin-orbit-torque memory operation of synthetic antiferromagnets, *Phys. Rev. Lett.* **121**, 167202 (2018).
- [36] T. Dohi, S. DuttaGupta, S. Fukami, and H. Ohno, Formation and current-induced motion of synthetic antiferromagnetic skyrmion bubbles, *Nat. Commun.* **10**, 5153 (2019).
- [37] J. Xia, X. Zhang, M. Ezawa, Z. Hou, W. Wang, X. Liu, and Y. Zhou, Current-driven dynamics of frustrated skyrmions in a synthetic antiferromagnetic bilayer, *Phys. Rev. Appl.* **11**, 044046 (2019).
- [38] W. Legrand, D. Maccariello, F. Ajejas, S. Collin, A. Vecchiola, K. Bouzehouane, N. Reyren, V. Cros, and A. Fert, Room-temperature stabilization of antiferromagnetic skyrmions in synthetic antiferromagnets, *Nat. Mater.* **19**, 34 (2020).
- [39] A. Salimath, F. Zhuo, R. Tomasello, G. Finocchio, and A. Manchon, Controlling the deformation of antiferromagnetic skyrmions in the high-velocity regime, *Phys. Rev. B* **101**, 024429 (2020).
- [40] S. Gao, H. D. Rosales, F. A. Gomez Albarracin, V. Tsurkan, G. Kaur, T. Fennell, P. Steffens, M. Boehm, P. Čermák, A. Schneidewind *et al.*, Fractional antiferromagnetic skyrmion lattice induced by anisotropic couplings, *Nature (London)* **586**, 37 (2020).

- [41] J. Xia, X. Zhang, K.-Y. Mak, M. Ezawa, O. A. Tretiakov, Y. Zhou, G. Zhao, and X. Liu, Current-induced dynamics of skyrmion tubes in synthetic antiferromagnetic multilayers, *Phys. Rev. B* **103**, 174408 (2021).
- [42] M. Mohylna, F. Gomez Albarracín, M. Žukovič, and H. D. Rosales, Spontaneous antiferromagnetic skyrmion/antiskyrmion lattice and spiral spin-liquid states in the frustrated triangular lattice, *Phys. Rev. B* **106**, 224406 (2022).
- [43] A. Aldarawsheh, I. L. Fernandes, S. Brinker, M. Sallermann, M. Abusaa, S. Blügel, and S. Lounis, Emergence of zero-field non-synthetic single and interchained antiferromagnetic skyrmions in thin films, *Nat. Commun.* **13**, 7369 (2022).
- [44] A. Aldarawsheh, M. Sallermann, M. Abusaa, and S. Lounis, A spin model for intrinsic antiferromagnetic skyrmions on a triangular lattice, *Front. Phys.* **11**, 1175317 (2023).
- [45] C. E. Barker, E. Haltz, T. Moore, C. H. Marrows *et al.*, Breathing modes of skyrmion strings in a synthetic antiferromagnet multilayer, *J. Appl. Phys.* **133**, 113901 (2023).
- [46] C. E. Barker, K. Fallon, C. Barton, E. Haltz, T. P. Almeida, S. Villa, C. Kirkbride, F. Maccherozzi, B. Sarpi, S. S. Dhese *et al.*, Phase coexistence and transitions between antiferromagnetic and ferromagnetic states in a synthetic antiferromagnet, *Phys. Rev. B* **109**, 134437 (2024).
- [47] A. Aldarawsheh, M. Sallermann, M. Abusaa, and S. Lounis, Current-driven dynamics of antiferromagnetic skyrmions: From skyrmion Hall effects to hybrid inter-skyrmion scattering, [arXiv:2403.01987](https://arxiv.org/abs/2403.01987).
- [48] T. Jungwirth, X. Marti, P. Wadley, and J. Wunderlich, Antiferromagnetic spintronics, *Nat. Nanotechnol.* **11**, 231 (2016).
- [49] M. Weißenhofer and U. Nowak, Temperature dependence of current-driven and Brownian skyrmion dynamics in ferrimagnets with compensation point, *Phys. Rev. B* **107**, 064423 (2023).
- [50] S. K. Kim, K.-J. Lee, and Y. Tserkovnyak, Self-focusing skyrmion racetracks in ferrimagnets, *Phys. Rev. B* **95**, 140404(R) (2017).
- [51] S. K. Kim, K. Nakata, D. Loss, and Y. Tserkovnyak, Tunable magnonic thermal Hall effect in skyrmion crystal phases of ferrimagnets, *Phys. Rev. Lett.* **122**, 057204 (2019).
- [52] S. Woo, K. M. Song, X. Zhang, Y. Zhou, M. Ezawa, X. Liu, S. Finizio, J. Raabe, N. J. Lee, S.-I. Kim *et al.*, Current-driven dynamics and inhibition of the skyrmion Hall effect of ferrimagnetic skyrmions in GdFeCo films, *Nat. Commun.* **9**, 959 (2018).
- [53] Y. Hirata, D.-H. Kim, S. K. Kim, D.-K. Lee, S.-H. Oh, D.-Y. Kim, T. Nishimura, T. Okuno, Y. Futakawa, H. Yoshikawa *et al.*, Vanishing skyrmion Hall effect at the angular momentum compensation temperature of a ferrimagnet, *Nat. Nanotechnol.* **14**, 232 (2019).
- [54] J. Brandão, D. Dugato, M. Puydinger dos Santos, and J. Cezar, Evolution of zero-field ferrimagnetic domains and skyrmions in exchange-coupled Pt/CoGd/Pt confined nanostructures: Implications for antiferromagnetic devices, *ACS Appl. Nano Mater.* **2**, 7532 (2019).
- [55] A.-O. Mandru, O. Yıldırım, R. Tomasello, P. Heistracher, M. Penedo, A. Giordano, D. Suess, G. Finocchio, and H. J. Hug, Coexistence of distinct skyrmion phases observed in hybrid ferromagnetic/ferrimagnetic multilayers, *Nat. Commun.* **11**, 6365 (2020).
- [56] O. Yıldırım, R. Tomasello, Y. Feng, G. Carlotti, S. Tacchi, P. M. Vaghefi, A. Giordano, T. Dutta, G. Finocchio, H. J. Hug *et al.*, Tuning the coexistence regime of incomplete and tubular skyrmions in ferromagnetic/ferrimagnetic/ferromagnetic trilayers, *ACS Appl. Mater. Interfaces* **14**, 34002 (2022).
- [57] L. Berges, E. Haltz, S. Panigrahy, S. Mallick, R. Weil, S. Rohart, A. Mougin, and J. Sampaio, Size-dependent mobility of skyrmions beyond pinning in ferrimagnetic GdCo thin films, *Phys. Rev. B* **106**, 144408 (2022).
- [58] X. Wang, A. R. Stuart, M. S. Swyt, C. M. Q. Flores, A. T. Clark, A. Fiagbenu, R. V. Chopdekar, P. N. Lapa, Z. Xiao, D. Keavney *et al.*, Topological spin memory of antiferromagnetically coupled skyrmion pairs in Co/Gd/Pt multilayers, *Phys. Rev. Mater.* **6**, 084412 (2022).
- [59] R. Bläsing, T. Ma, S.-H. Yang, C. Garg, F. K. Dejene, A. T. N'Diaye, G. Chen, K. Liu, and S. S. Parkin, Exchange coupling torque in ferrimagnetic Co/Gd bilayer maximized near angular momentum compensation temperature, *Nat. Commun.* **9**, 4984 (2018).
- [60] M. A. Müller, Modelling SOT-driven domain wall motion in Pt/Co/Gd multilayers with Mumax3, Master's thesis, Eindhoven University of Technology, 2021.
- [61] P. Li, T. J. Kools, B. Koopmans, and R. Lavrijsen, Ultrafast race-track based on compensated Co/Gd-based synthetic ferrimagnet with all-optical switching, *Adv. Electron. Mater.* **9**, 2200613 (2023).
- [62] D. Das, Y. Cen, J. Wang, and X. Fong, Bilayer-skyrmion-based design of neuron and synapse for spiking neural network, *Phys. Rev. Appl.* **19**, 024063 (2023).
- [63] Y. Shen, C. He, Z. Song, B. Chen, H. He, Y. Ma, J. A. Fells, S. J. Elston, S. M. Morris, M. J. Booth *et al.*, Topologically controlled multiskyrmions in photonic gradient-index lenses, *Phys. Rev. Appl.* **21**, 024025 (2024).
- [64] C. S. Davies and V. Kruglyak, Graded-index magnonics, *Low Temp. Phys.* **41**, 760 (2015).
- [65] C. Davies, A. Francis, A. Sadovnikov, S. Chertopalov, M. Bryan, S. Grishin, D. Allwood, Y. P. Sharavskii, S. Nikitov, and V. Kruglyak, Towards graded-index magnonics: Steering spin waves in magnonic networks, *Phys. Rev. B* **92**, 020408 (2015).
- [66] C. Davies, V. Poimanov, and V. Kruglyak, Mapping the magnonic landscape in patterned magnetic structures, *Phys. Rev. B* **96**, 094430 (2017).
- [67] R. Tomasello, S. Komineas, G. Siracusano, M. Carpentieri, and G. Finocchio, Chiral skyrmions in an anisotropy gradient, *Phys. Rev. B* **98**, 024421 (2018).
- [68] L. Shen, J. Xia, G. Zhao, X. Zhang, M. Ezawa, O. A. Tretiakov, X. Liu, and Y. Zhou, Dynamics of the antiferromagnetic skyrmion induced by a magnetic anisotropy gradient, *Phys. Rev. B* **98**, 134448 (2018).
- [69] I. R. de Assis, I. Mertig, and B. Göbel, Skyrmion motion in magnetic anisotropy gradients: Acceleration caused by deformation, *Phys. Rev. B* **108**, 144438 (2023).
- [70] O. Udalov, I. Beloborodov, and M. Sapozhnikov, Magnetic skyrmions and bimerons in films with anisotropic interfacial Dzyaloshinskii-Moriya interaction, *Phys. Rev. B* **103**, 174416 (2021).
- [71] M. Sapozhnikov, R. Gorev, E. Skorokhodov, N. Gusev, A. Sadovnikov, and O. Udalov, Zigzag domains caused by strain-induced anisotropy of the Dzyaloshinskii-Moriya interaction, *Phys. Rev. B* **105**, 024405 (2022).

- [72] I. O. Gorshkov, R. V. Gorev, M. V. Sapozhnikov, and O. G. Udalov, DMI-gradient-driven skyrmion motion, *ACS Appl. Electron. Mater.* **4**, 3205 (2022).
- [73] M. Vogel, R. Aßmann, P. Pirro, A. V. Chumak, B. Hillebrands, and G. von Freymann, Control of spin-wave propagation using magnetisation gradients, *Sci. Rep.* **8**, 11099 (2018).
- [74] P. Borys, N. Qureshi, C. Ordóñez-Romero, and O. Kolokoltsev, Scattering of exchange spin waves from regions of modulated magnetization, *Europhys. Lett.* **128**, 17003 (2019).
- [75] R. Gallardo, P. Alvarado-Seguel, T. Schneider, C. Gonzalez-Fuentes, A. Roldán-Molina, K. Lenz, J. Lindner, and P. Landeros, Spin-wave non-reciprocity in magnetization-graded ferromagnetic films, *New J. Phys.* **21**, 033026 (2019).
- [76] S. Mieszczak, O. Busel, P. Gruszecki, A. N. Kuchko, J. W. Kłos, and M. Krawczyk, Anomalous refraction of spin waves as a way to guide signals in curved magnonic multimode waveguides, *Phys. Rev. Appl.* **13**, 054038 (2020).
- [77] P. Borys, O. Kolokoltsev, N. Qureshi, M. Plumer, and T. Monchesky, Unidirectional spin wave propagation due to a saturation magnetization gradient, *Phys. Rev. B* **103**, 144411 (2021).
- [78] O. Kolokoltsev, N. Qureshi, E. Mejía-Urriarte, and C. L. Ordóñez-Romero, Hot spin-wave resonators and scatterers, *J. Appl. Phys.* **112**, 013902 (2012).
- [79] M. Vogel, A. V. Chumak, E. H. Waller, T. Langner, V. I. Vasyuchka, B. Hillebrands, and G. von Freymann, Optically reconfigurable magnetic materials, *Nat. Phys.* **11**, 487 (2015).
- [80] R. Tomasello, E. Martinez, R. Zivieri, L. Torres, M. Carpentieri, and G. Finocchio, A strategy for the design of skyrmion racetrack memories, *Sci. Rep.* **4**, 6784 (2014).
- [81] S. Zhang and Z. Li, Roles of nonequilibrium conduction electrons on the magnetization dynamics of ferromagnets, *Phys. Rev. Lett.* **93**, 127204 (2004).
- [82] Y. Yamane, J. Ieda, and J. Sinova, Spin-transfer torques in antiferromagnetic textures: Efficiency and quantification method, *Phys. Rev. B* **94**, 054409 (2016).
- [83] J. C. Slonczewski, Current-driven excitation of magnetic multilayers, *J. Magn. Magn. Mater.* **159**, L1 (1996).
- [84] A. Vansteenkiste, J. Leliaert, M. Dvornik, M. Helsen, F. Garcia-Sanchez, and B. Van Waeyenberge, The design and verification of MuMax3, *AIP Adv.* **4**, 107133 (2014).
- [85] M. Laliou, M. Peeters, S. Haenen, R. Lavrijsen, and B. Koopmans, Deterministic all-optical switching of synthetic ferromagnets using single femtosecond laser pulses, *Phys. Rev. B* **96**, 220411 (2017).
- [86] X. Wang, H. Yuan, and X. Wang, A theory on skyrmion size, *Commun. Phys.* **1**, 31 (2018).
- [87] M. Morota, Y. Niimi, K. Ohnishi, D. Wei, T. Tanaka, H. Kontani, T. Kimura, and Y. Otani, Indication of intrinsic spin Hall effect in *4d* and *5d* transition metals, *Phys. Rev. B* **83**, 174405 (2011).
- [88] M. Beg, R. Carey, W. Wang, D. Cortés-Ortuño, M. Vousden, M.-A. Bisotti, M. Albert, D. Chernyshenko, O. Hovorka, R. L. Stamps *et al.*, Ground state search, hysteretic behaviour and reversal mechanism of skyrmionic textures in confined helimagnetic nanostructures, *Sci. Rep.* **5**, 17137 (2015).
- [89] A. Thiele, Steady-state motion of magnetic domains, *Phys. Rev. Lett.* **30**, 230 (1973).